

Plasmon-Enhanced Catalysis: Distinguishing Thermal and Nonthermal Effects

Xiao Zhang,[†] Xueqian Li,[†] Matthew E. Reish,[‡] Du Zhang,[†] Neil Qiang Su,[†] Yael Gutiérrez,[§] Fernando Moreno,[§] Weitao Yang,^{†,||} Henry O. Everitt,^{‡,||} and Jie Liu^{*,†,||}

[†]Department of Chemistry, Duke University, Durham, North Carolina 27708, United States

[‡]Army Aviation & Missile RD&E Center, Redstone Arsenal, Alabama 35898, United States

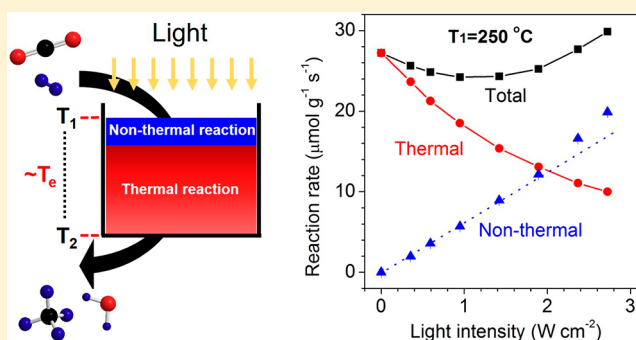
[§]Optics Group, Department of Applied Physics, University of Cantabria, Avda de Los Castros, s/n 39005 Santander, Spain

^{||}Department of Physics, Duke University, Durham, North Carolina 27708, United States

Supporting Information

ABSTRACT: In plasmon-enhanced heterogeneous catalysis, illumination accelerates reaction rates by generating hot carriers and hot surfaces in the constituent nanostructured metals. In order to understand how photogenerated carriers enhance the nonthermal reaction rate, the effects of photo-thermal heating and thermal gradients in the catalyst bed must be confidently and quantitatively characterized. This is a challenging task considering the conflating effects of light absorption, heat transport, and reaction energetics. Here, we introduce a methodology to distinguish the thermal and nonthermal contributions from plasmon-enhanced catalysts, demonstrated by illuminated rhodium nanoparticles on oxide supports to catalyze the CO₂ methanation reaction. By simultaneously measuring the total reaction rate and the temperature gradient of the catalyst bed, the effective thermal reaction rate may be extracted. The residual nonthermal rate of the plasmon-enhanced reaction is found to grow with a superlinear dependence on illumination intensity, and its apparent quantum efficiency reaches ~46% on a Rh/TiO₂ catalyst at a surface temperature of 350 °C. Heat and light are shown to work synergistically in these reactions: the higher the temperature, the higher the overall nonthermal efficiency in plasmon-enhanced catalysis.

KEYWORDS: Plasmon, photocatalyst, rhodium nanoparticles, heterogeneous catalysis, carbon dioxide reduction



Light absorbed by metal nanostructures through intraband or interband transitions excites hot carriers or electron hole pairs, respectively. Particularly strong light-matter interactions are observed when collective oscillations of free electrons, called localized surface plasmons (LSPs), are excited.¹ Photoexcitation generates mobile free carriers, and electron-phonon scattering generates heat, both of which contribute to the catalytic activity of these nanostructures. Recently, the plasmonic community has generated excitement by demonstrating that the transfer of hot carriers into antibonding orbitals of surface adsorbates at the rate-determining step (RDS) may select products and accelerate chemical reactions by weakening certain chemical bonds.^{2–7} By catalyzing reactions under mild conditions, plasmon-enhanced catalysis offers a compelling remedy to the exorbitant energy requirements of traditional thermal catalysis while simultaneously extending the lifetime of catalysts.^{8,9} However, absorbed light also heats these metal nanoparticles, so claims about the beneficial effects of hot carriers must first convincingly distinguish the effects of “nonthermal” hot carriers from those of “thermal” hot surfaces. Unfortunately, it is quite difficult to measure the temperature of individual metal

nanoparticles, so this discrimination has primarily depended on calculations that estimate the degree of photothermal heating or on simple measurements of the catalyst’s thermal activity prior to illumination.

Here we demonstrate a more comprehensive experimental exploration and discrimination of thermal and nonthermal catalytic activities under illumination. Our exploration uses rhodium (Rh) nanoparticles, already well-known as an effective thermal catalyst^{10–15} and recently demonstrated as an effective plasmon-enhanced catalyst through the discovery of its ultraviolet (UV) plasmonic behavior.^{16–19} Specifically, the carbon dioxide (CO₂) hydrogenation reaction is investigated, and by using much smaller Rh nanoparticles on a more active titanium dioxide (TiO₂) support, we dramatically enhance the activity of the catalyst to create conditions under which thermal and nonthermal catalytic behaviors are at work simultaneously and cooperatively. Measurements and a model describing the temperature profile of the catalyst bed are proposed to obtain

Received: November 11, 2017

Revised: January 29, 2018

Published: February 13, 2018

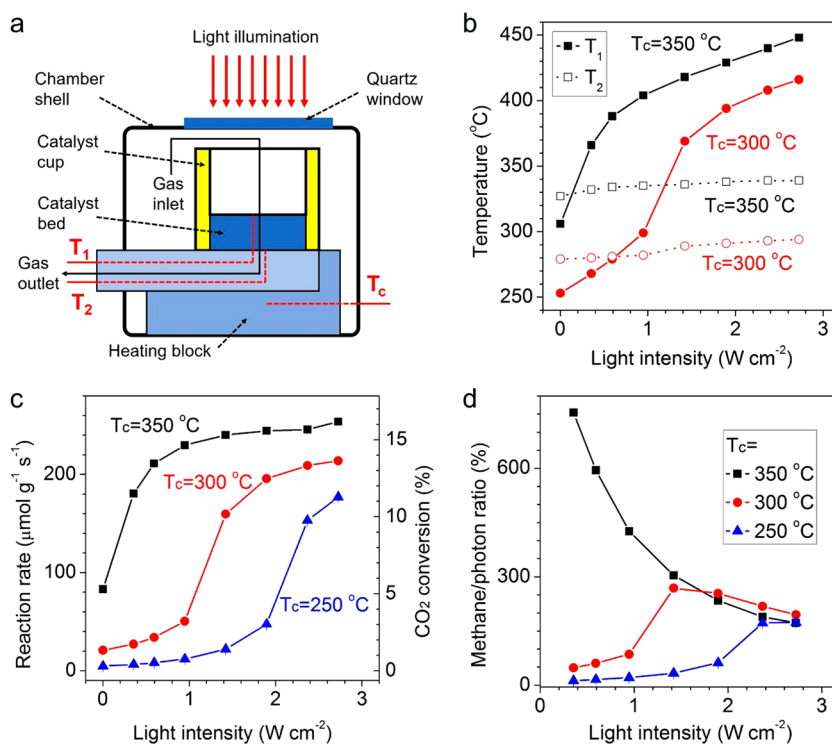


Figure 1. (a) Schematic representation of the modified reaction chamber for in situ measurements of top- (T_1) and bottom- (T_2) surface temperatures of the catalyst bed. Chamber temperature (T_c) is measured by a thermocouple underneath the catalyst cup inside the heating block. (b) Measured T_1 (solid symbols) and T_2 (open symbols) at $T_c = 350^{\circ}\text{C}$ (black squares) and 300°C (red circles) as a function of I_{uv} . (c) Measured total reaction rates and CO_2 conversion at $T_c = 350^{\circ}\text{C}$ (black squares), 300°C (red circles), and 250°C (blue triangles) as a function of I_{uv} . (d) Methane/photon ratios at the same T_c temperatures as a function of I_{uv} . The methane/photon ratio is calculated as the difference between methane production rate under light and in the dark at the same T_c , divided by photon flux. The reactions are carried out with a ~ 3 mm thick Rh-s/ TiO_2 catalyst and 50 sccm CO_2 , 150 sccm H_2 , and 50 sccm Ar. Error bars are smaller than symbols and represent the standard deviation of measurements by the mass spectrometer.

the effective thermal and nonthermal reaction rates under illumination with and without external heating. The nonthermal reaction rate shows a reduced apparent activation energy and a superlinear dependence on light intensity, both signatures of hot-electron-driven reactions. The methodology by which we discriminate thermal and nonthermal contributions and extract the reaction rate and efficiency of hot-electron-driven reactions may be applied universally to any explorations of plasmon-enhanced catalysis. Our analysis affirms that plasmonic behavior provides new control over the catalytic behaviors of metal nanostructures when the mechanism is thermal, nonthermal, or both.

A commercial photoreactor (Harrick HVC-MRA-5, Figure 1a) with a quartz optical window contained the 3 mm thick catalyst bed composed of 6 nm diameter spherical Rh nanoparticles on a TiO_2 powder support (Rh-s/ TiO_2 , details in Supporting Information, Figure S1, for morphology and Methods for synthesis). The chamber temperature (T_c) is monitored within the heating block of the chamber by a thermocouple provided by the manufacturer. In previously reported investigations of plasmon-enhanced catalysis, T_c is used as the set point and assumed to represent the isothermal temperature of the catalyst bed. However, illumination, external heating, gas flow, and reaction energetics produce thermal gradients in the catalyst. To measure its temperature profile, we embedded two thin gauge thermocouples (~ 0.5 mm sheath diameter) in the catalyst bed through the gas outlet port of the photoreactor (Figure 1a), one buried within 0.1 mm of the top surface to measure the top temperature (T_1) and the other at

the bottom to measure the bottom temperature (T_2). Figure 1b illustrates the dependence of T_1 and T_2 on illumination intensity by a modest intensity UV light-emitting diode (LED, $I_{\text{uv}} < 3 \text{ W/cm}^2$, 365 nm) with a ~ 3 mm thick Rh-s/ TiO_2 catalyst thermostatically held at $T_c = 300$ and 350°C using 50 standard cubic centimeters per minute (sccm) CO_2 , 150 sccm H_2 , and 50 sccm Ar. The flowing gas produces $T_2 < T_c$ for all light intensities while T_1 increases rapidly from below to well above T_c with increasing light intensity. Temperature gradients $> 100^{\circ}\text{C}$ across a 3 mm thick catalyst are observed at the highest light intensity, so the set point temperature T_c neither represents the average temperature nor the thermal profile of the catalyst.

On the Rh-s/ TiO_2 catalyst, CO_2 methanation ($\text{CO}_2 + 4\text{H}_2 \rightarrow \text{CH}_4 + 2\text{H}_2\text{O}$) is the dominant reaction pathway, and the product selectivity toward methane (CH_4) is greater than 98% in both dark and light conditions (Supporting Information, Figure S2a). For a given T_c , the CH_4 reaction rates exhibit monotonic increases with increasing I_{uv} (Figure 1c) until plateauing (e.g., $I_{\text{uv}} \approx 0.6 \text{ W cm}^{-2}$ for $T_c = 350^{\circ}\text{C}$) because the reaction becomes diffusion limited (i.e., CO_2 conversion $> 10\%$). Prior experimental and theoretical investigations of the reaction mechanism on supported Rh and ruthenium catalysts suggest that CO_2 first dissociatively adsorbs as CO and O, then CO is hydrogenated to CHO.^{14,15,20–24} The dissociation of CH–O into CH and O is identified to be the RDS of CO_2 methanation, followed by fast hydrogenation of CH to produce CH_4 . (See the Supporting Information for details.)

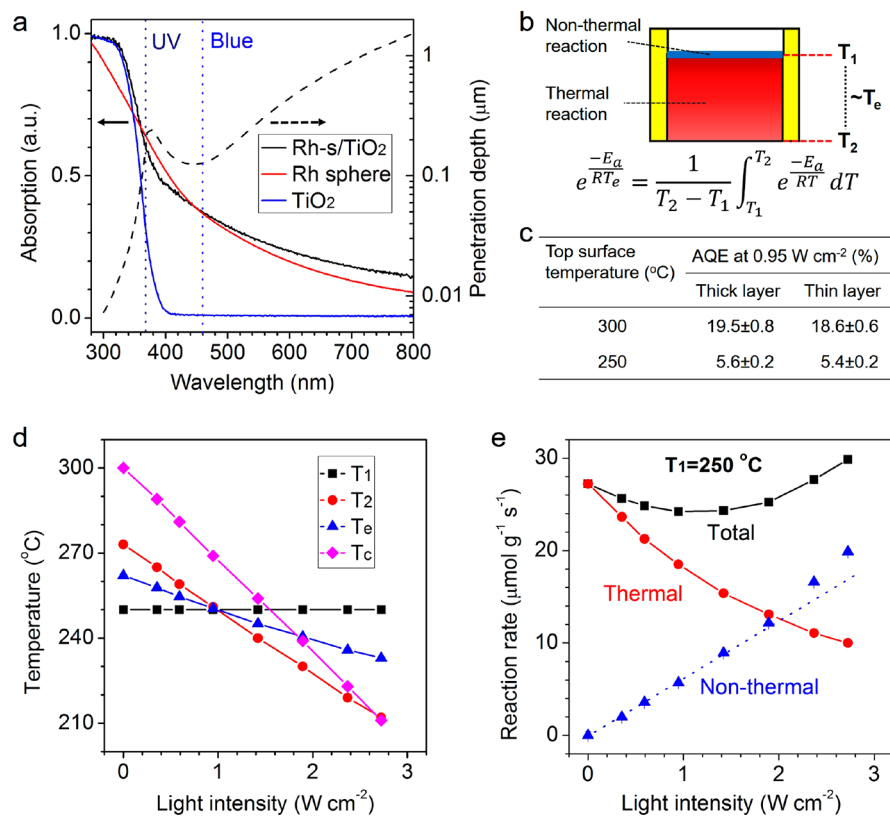


Figure 2. (a) Measured absorbance (solid lines) of Rh-s/TiO₂ (black), Rh-s in an ethanol solution (red), and pure TiO₂ support (blue), overlaid with the estimated penetration depth of Rh-s/TiO₂ (black dotted line). Vertical lines show the central wavelengths of the UV and blue LEDs. (b) Temperature gradient model of the catalyst bed and the equation to calculate equivalent temperature T_e from T_1 and T_2 . The nonthermal reaction only occurs in the top illuminated part of the catalyst bed, while thermal reaction occurs throughout. The figure is not to scale. (c) AQE from a ~ 3 mm and a ~ 1 mm thick Rh-s/TiO₂ catalyst for $T_1 = 300$ and 250 °C for $I_{uv} = 0.95$ W cm⁻². (d) T_1 (black squares), T_2 (red circles), T_e (blue triangles), and T_c (magenta diamonds) of a ~ 1 mm thick of Rh-s/TiO₂ catalyst at $T_1 = 250$ °C as a function of I_{uv} . (e) Total (black squares), thermal (red circles), and nonthermal (blue triangles) reaction rates at $T_1 = 250$ °C as a function of I_{uv} . The nonthermal reaction rate is the difference between the total and effective thermal reaction rates. The reactions are carried out with 50 sccm CO₂, 150 sccm H₂, and 50 sccm Ar. Error bars are smaller than symbols and represent the standard deviation of measurements by the mass spectrometer.

The observed photoenhanced reaction rate includes both “thermal” and “nonthermal” contributions, but how may these be parsed? An important clue comes from the methane/photon ratio, commonly defined as the difference in the illuminated and unilluminated reaction rates at a common chamber temperature divided by the photon flux.^{4,25} Using this definition, we measure a methane/photon ratio as large as $\sim 800\%$ under low-intensity UV illumination ($I_{uv} \approx 0.4$ W cm⁻²) with $T_c = 350$ °C (Figure 1d). This clearly seems unphysical, as if each photon creates a hot carrier that breaks bonds of as many as eight different intermediate adsorbates at the RDS.^{26–28} Furthermore, this ratio decreases with increasing light intensity, as if adding more photons makes the reaction less efficient. The only explanation is that somehow the subtraction of thermal effects was incomplete. Indeed, the critical assumption that illumination only generates nonthermal contributions is incorrect because it omits the effects of photothermal heating and the associated thermal gradient, effects clearly seen in Figure 1b. Thus, to ascertain the extent of any nonthermal contributions, the reaction rate caused by photothermal heating must also be characterized and subtracted, just as the reaction rate for unilluminated thermal heating was.

Our proposed method for separating the photothermal and nonthermal contributions of the reaction rate first considers the

wavelength-dependent light penetration depth of the catalyst constituents. The ~ 3 eV (413 nm) bandgap of rutile TiO₂ strongly absorbs light from the “UV” LED (365 nm) but is transparent to the “blue” LED (460 nm) used. While the LSP of Rh spheres in an ethanol suspension has its peak in the deep UV region (>6 eV), the broad tail of its resonance extends well into the blue/violet spectral region and absorbs light from both LEDs.^{17–19} Thus, the intraband absorption of UV and blue illumination by the Rh nanoparticles nonresonantly excites this LSP and generates hot electrons with a nearly free-electron behavior.^{16,29} The light penetration depth into the Rh-s/TiO₂ catalyst, modeled as a uniform distribution of Rh nanoparticles on a continuous TiO₂ host with the correct 5:95 mass ratio of constituents, is only ~ 0.1 μ m for both LEDs (Figure 2a, details for calculation method in Supporting Information), indicating that the absorption is dominated by the Rh nanoparticles. Even if the porous structure of the TiO₂ support and the light scattering at the gas–solid interface were considered, the 3 mm thick Rh-s/TiO₂ catalyst still absorbs all illumination in much less than 1 μ m. Obviously, nonthermal reactions requiring direct light–matter interactions, which involve hot-electron-driven reactions,^{4,5} photomodification of the catalyst,³⁰ and enhanced near field effects,¹⁸ can only occur in this thin layer, and the temperature of that thin layer is best represented by T_1 (blue area in Figure 2b).

Of course, thermal reactions can occur throughout the catalyst bed and only depend on the temperature of catalyst, regardless of the source of heat (red area in Figure 2b). This is even true for photothermal heating because the thermal conductivities of the catalyst and flowing gases transport surface heating throughout. Note that thermal and nonthermal reactions are defined by their respective reaction mechanisms, regardless of their location in the catalyst bed. Moreover, the local temperature within the catalyst generally increases with increasing illumination but decreases with increasing gas flow and may further increase or decrease depending on how exothermic or endothermic the reaction is. Consequently, the temperature profile in the catalyst evolves in a complex, dynamical manner as a function of many factors.

To capture this, we propose a model with a vertical temperature gradient within the catalyst bed. Under steady-state conditions, a linear vertical temperature gradient approximation captures the excellent thermal conduction throughout both the catalyst bed and the gaseous reaction mixture, while the uniform illumination of the catalyst requires no horizontal gradient. Since the relationship between the thermal reaction rate and the reaction temperature follows an Arrhenius equation under conditions of low reactant conversion (<10%), an equivalent temperature T_e , defined through the relationship

$$e^{-E_a/kT_e} = \frac{1}{T_2 - T_1} \int_{T_1}^{T_2} e^{-E_a/kT} dT \quad (1)$$

conveniently describes the overall reactivity of thermal reactions in a catalyst bed with temperature gradients in both dark and light conditions. Due to the interdependent relationship of T_e and the apparent activation energy E_a , the equation is solved by an iterative method using the measured T_1 , T_2 , and dark thermal reaction rate. (See the Supporting Information for details.) Once E_a is obtained, the total thermal contribution from the LED, the heater, and the exothermic reaction itself is captured by measuring the new T_1 and T_2 values upon illumination, from which the new T_e and thermal reaction rate may be calculated. In this manner, the effective thermal reaction rate (R_t) may be characterized and subtracted from the total measured reaction rate so that the nonthermal reaction rate (R_{nt}) may be confidently known and explored.

Before using this methodology, we must address the issue of quantum efficiency. Since nonthermal reactions are limited to the top layer of the catalyst bed, reaction rates normalized to the total weight of the catalyst bed do not properly represent the intrinsic nonthermal catalytic activity, especially comparing the performance of different catalysts. Instead, we introduce an apparent quantum efficiency (AQE), defined as the ratio of the deduced nonthermal rate to the photon flux delivered to catalyst, assuming that all nonthermal reactions are driven by the transfer of photogenerated hot electrons. The AQE, which may be used to evaluate the efficiency of plasmon-enhanced catalysis, does not involve and should be independent of the total weight (thickness) of catalyst. We confirm this expectation through measurements and calculations of nonthermal AQE using thick (~ 3 mm thickness) and thin (~ 1 mm thickness) layers of Rh-s/TiO₂ catalyst (Figure 2c). The fact that they are the same to within experimental uncertainty validates the ability of our model to ascertain the effective thermal reaction rate and extract the real contribution from nonthermal reactions. To maintain a low conversion of reactants and minimize the

temperature gradient in the catalyst bed, a thin layer (~ 1 mm) of catalyst is used in the following experiments.

To explore the mechanism for the nonthermal contribution, we begin by investigating the dependence of R_{nt} on light intensity with 50 sccm CO₂, 150 sccm H₂, and 50 sccm Ar.³¹ These experiments were carried out by fixing not T_c but the top-surface temperature $T_1 = 250$ °C, since T_1 describes the temperature where nonthermal reaction occurs. As I_{uv} increased, both T_2 and T_c decreased as photothermal heating of the top surface caused the thermostat to reduce T_c to maintain T_1 (Figure 2d). The resulting T_e decreased at first, explaining why R_t and the total reaction rate actually slowed as I_{uv} increased (Figure 2e). However, as I_{uv} grew even higher, the total reaction rate began to increase, even though T_e and R_t continued to drop. It became increasingly apparent that R_{nt} , calculated as the difference between the measured total reaction rate and the deduced R_t , had begun to make a larger contribution as the reaction evolved from a thermal-dominated to nonthermal-dominated mechanism. Indeed, the R_{nt} exhibited a superlinear dependence on I_{uv} , a signature consistent with hot-electron-driven reactions that are the likely nonthermal mechanism in the present system.^{4,32,33} Moreover, the AQE calculated from this nonthermal mechanism was a much more physically reasonable $\sim 6\%$ and relatively independent of I_{uv} in the low light intensity regime, a further indication that the thermal effects have been correctly accounted and the remaining nonthermal mechanism is caused by the plasmonic generation and transfer of hot electrons. Of course, only a fraction of the absorbed photons generate hot electrons for nonthermal reactions, but all absorbed light energy eventually heats the catalyst through electron–phonon scattering.

Suppose this subtraction of thermal effects was incomplete, that residual photothermal effects caused R_t to be underestimated and R_{nt} to be overestimated under illumination. Consider the two most likely concerns: T_1 only measures the temperature of the TiO₂ support but the illuminated Rh nanoparticles are hotter, or T_1 is lower than the temperature at the very top surface of the catalyst bed since the thermocouple tip is covered by catalyst to avoid direct photoheating of the thermocouple. In the first case, the high thermal conductivity of the Rh NPs, the TiO₂ support, and the flowing gas (especially H₂) prevent a local thermal gradient larger than 0.1 °C.⁴ As for the second case, the linear dependence of T_2 on I_{uv} for constant T_1 (Figure 2d) suggests the top-surface temperature should also increase linearly above T_1 . However, the high thermal conductivity limits the measured thermal gradient to <40 mK/ μ m (Figure 2d), which prevents this top temperature from rising much above T_1 (<4 °C). Moreover, any temperature rise would produce an Arrhenius-type exponential dependence of R_{nt} on light intensity that is inconsistent with the observed linear to superlinear dependence. Therefore, the majority of the calculated residual R_{nt} cannot be due to an underestimation of R_t . The consistent nonthermal AQE for both thick and thin catalyst beds further proves R_t was appropriately measured and subtracted with our proposed model.

Thus, with an appropriate method to extract R_{nt} and AQE of plasmon-enhanced CO₂ methanation, experiments were carried out over a range of fixed T_1 from 200 to 300 °C. In every case, R_{nt} and resulting AQE increased with increasing T_1 . R_{nt} increased superlinearly with increasing I_{uv} (Figure 3a), while the AQE was relatively insensitive to I_{uv} (Figure 3b). For a further increase of $T_1 = 350$ °C and $I_{UV} = 2.7$ W cm⁻², the measured AQE reached $\sim 46\%$, somewhat higher than the

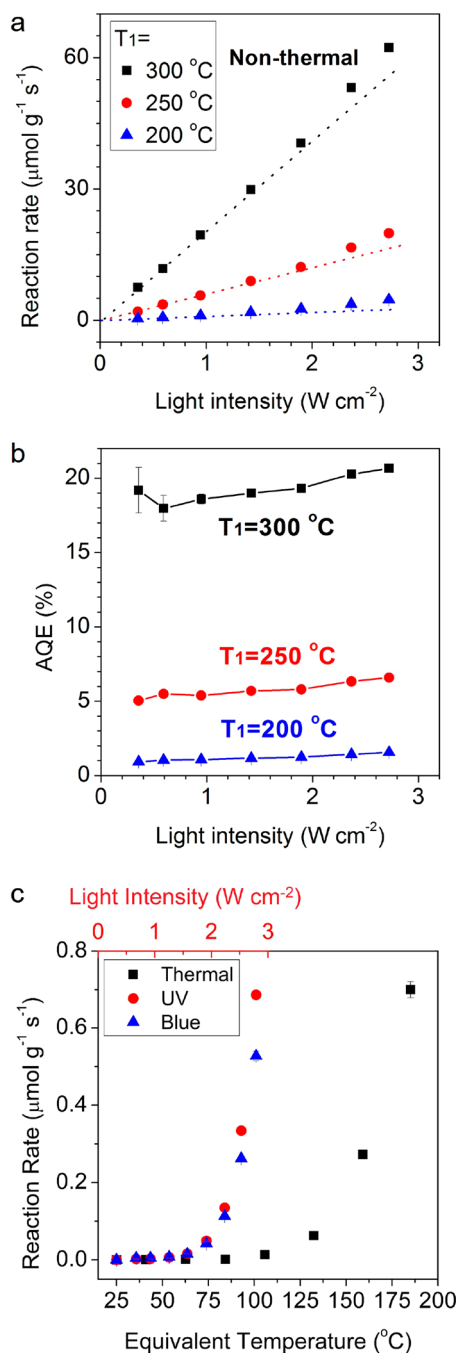


Figure 3. (a) Nonthermal reaction rates and (b) AQE for $T_1 = 300^\circ\text{C}$ (black squares), 250°C (red circles), and 200°C (blue triangles) as a function of I_{UV} . (c) Overall low temperature reaction rates for dark heating conditions (black squares) and under UV (red circles) and blue illumination (blue triangles) without additional heating, plotted as a function of equivalent temperature and light intensity (secondary x-axis). The reactions are carried out with 50 sccm CO_2 , 150 sccm H_2 , and 50 sccm Ar. Error bars represent the standard deviations of measurements by the mass spectrometer.

efficiencies of previous reports of plasmon-enhanced catalysis and plasmonic-hot-electron-based devices.^{25,31,34–37} While much lower than the $\sim 800\%$ efficiency calculated without including photothermal heating, the activity of the Rh-s/ TiO_2 catalyst clearly grew quite high under moderate UV illumination. These findings indicate a cooperative role between

light and heat that distinguishes plasmon-enhanced catalysis from traditional photocatalysis.

Further understanding of the nonthermal reaction mechanism may be obtained under blue illumination, which cannot be absorbed by the TiO_2 support but still can be absorbed by the Rh nanoparticles. As with UV illumination, the nonthermal reaction rate increases with a superlinear dependence on I_{blue} , and the AQE is only slightly lower than that under UV illumination at the same intensity (Supporting Information, Figure S3). Together, these indicate that the Rh nanoparticles, not the TiO_2 support, are responsible for the nonthermal photoinduced reaction and provide further evidence of mediation by hot electrons.

Experiments were also carried out near room temperature where thermal reaction rates are negligible. For both blue and UV illumination, light-induced CO_2 methanation begins at $T_e \sim 75^\circ\text{C}$, far less than the $T_e \sim 130^\circ\text{C}$ needed under dark thermal conditions (Figure 3c and Supporting Information, Figure S8). Given the high thermal conductivity of the catalyst and flowing gases, this large temperature difference for equivalent reactivity cannot be explained as a purely thermal effect, nor can it explain how much more rapidly the reaction rate increases with increasing illumination intensity than with increasing dark heating. Instead, these observations confirm the nonthermal nature of both the reaction and the synergistic way of photothermal heating and nonthermal processes cooperate.

Clues about the origin of the high AQE from the Rh-s/ TiO_2 catalyst come from measurements of the activation energies and the CO_2 and H_2 reaction orders for both thermal and nonthermal reactions, as well as their dependence on the support materials. To measure how both reaction rates depend on temperature and CO_2 or H_2 partial pressure, experiments were performed with a constant T_e for the thermal reactions, since these occur throughout the catalyst, and a constant T_1 for the nonthermal reactions, since these occur only on the top of the catalyst. The effective thermal reaction rates are calculated from T_e and subtracted from the total reaction rates to obtain the nonthermal reaction rates and AQE.

Both R_t and nonthermal AQE depend exponentially on temperature and may be characterized by an Arrhenius equation to extract the associated activation energies E_a . The thermal activation energy for the Rh-s/ TiO_2 catalyst is found to be $E_a = 77.5 \pm 0.1 \text{ kJ mol}^{-1}$ (Figure 4a), a value consistent with prior measurements.^{14,23} However, the nonthermal activation energy is only $58.3 \pm 0.7 \text{ kJ mol}^{-1}$ in the temperature range $200\text{--}300^\circ\text{C}$ (Figure 4b), indicating that the nonthermal mechanism more effectively weakens the chemical bond of the critical RDS intermediate, likely by transferring hot electrons to the intermediate and lowering E_a . At T_1 of 350°C , the measured AQE is lower than the extrapolated fit of the lower temperature data, indicating the expected plateauing of AQE as temperature increases further. As noted above, T_e and T_1 are the temperatures used in the Arrhenius equations to obtain the apparent E_a values for the thermal and nonthermal reactions, respectively.

Given that support materials offer much more than passive mechanical and thermal stabilizations of the metal nanoparticles in catalytic processes,^{14,24,38} we considered the effect of catalyst supports on the thermal and nonthermal reaction rate by comparing the activities of larger Rh nanocubes (35 nm edges) on Al_2O_3 and TiO_2 supports (Rh-c/ Al_2O_3 and Rh-c/ TiO_2) with similar Rh mass loadings. Consistent with previous reports, the TiO_2 -supported Rh catalyst exhibited a much higher

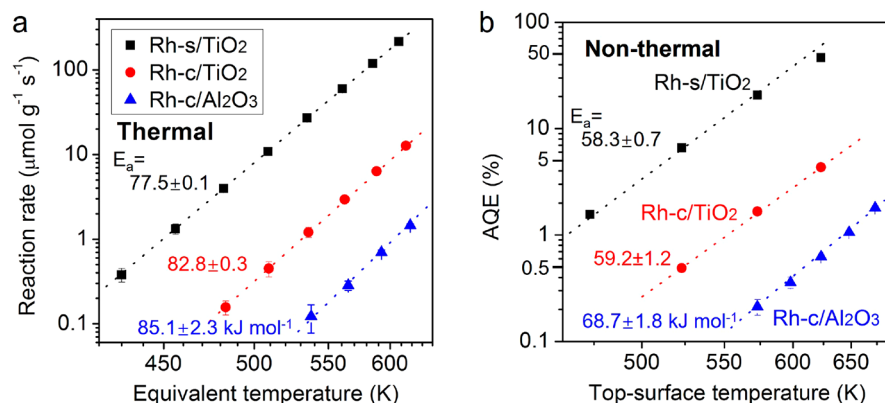


Figure 4. (a) Thermal reaction rates using Rh-s/TiO₂ (black squares), Rh-c/TiO₂ (red circles), and Rh-c/Al₂O₃ (blue triangles) catalysts as a function of T_e . (b) Nonthermal AQE using the same catalysts for $I_{uv} = 2.72 \text{ W cm}^{-2}$ as a function of T_1 . The reactions are carried out with 50 sccm CO₂, 150 sccm H₂, and 50 sccm Ar. Error bars represent the standard deviation of measurements by the mass spectrometer.

thermocatalytic activity and slightly lower activation energies than the Al₂O₃-supported catalyst for both thermal and nonthermal reactions (Figure 4). Indeed, E_a of the nonthermal reaction is always lower than E_a of the thermal reaction for all three catalysts, indicating that the nonthermal mechanism, perhaps hot-electron transfer to the critical intermediate at the RDS, lowers E_a beyond the thermal E_a . The fact that the nonthermal E_a 's for both Rh-TiO₂ catalysts are identical to within experimental uncertainty offers one more piece of evidence that the thermal contributions have been correctly subtracted and that the residual behaviors truly characterize the nonthermal reaction.

It is important to note that the reactivity comes almost entirely from the metal nanoparticles: control experiments on pure Al₂O₃ supports did not yield any detectable products under both dark and light conditions, while TiO₂ only showed a small response to UV light with CO as the product ($<0.01 \mu\text{mol g}^{-1} \text{s}^{-1}$). Moreover, the Rh-c/Al₂O₃ catalyst did not select for CH₄ under thermal conditions as effectively as either TiO₂-supported catalyst (Supporting Information, Figure S2). This has been attributed to highly active sites at the interface between Rh and reducible TiO₂,^{14,23,38} in particular, the interaction between the O atom in CHO intermediates and the reduced Ti³⁺ centers can weaken the C–O bond and facilitate the production of CH₄. It was recently demonstrated that nonthermal plasmon-enhanced hot electron effects dramatically improve the selectivity of the Rh-c/Al₂O₃ catalyst toward CH₄,¹⁶ but Figure 4 shows that both TiO₂-supported Rh catalysts exhibit higher nonthermal activities than the Al₂O₃-supported catalyst. This suggests that the benefits of highly active sites at the Rh-TiO₂ interface surpass the drawback of trapping hot electrons in TiO₂ for these plasmon-enhanced catalysts.²⁵ Indeed, photomodification of the Rh-TiO₂ interface may be another possible nonthermal effect to be investigated.

Regarding the CO₂ and H₂ reaction orders, the different thermal conductivities of the reactant gases (33.5 and 272 mW m⁻¹ K⁻¹ at 227 °C for CO₂ and H₂, respectively) produce temperature gradients within the catalyst bed that evolve as the partial pressures are varied. To extract the reaction order, the results are plotted in double logarithmic scales and fitted with

$$R = k p_{\text{CO}_2}^x p_{\text{H}_2}^y \quad (2)$$

where p_{CO_2} and p_{H_2} are the partial pressures of CO₂ and H₂ with reaction orders x and y , respectively. Positive reaction orders

indicate the reaction is starved for that reactant, accelerating as additional gas is provided, while negative reaction orders indicate the reaction quenches as additional reactant is added.

Thermal reactions, respectively, exhibit reaction orders of $x = 0.12$ and $y = 0.34$ for CO₂ and H₂ at $T_e = 313 \text{ °C}$ (Figure 5a,c), values close to previous reports on supported Rh catalysts.¹⁴ Both reactions accelerate with increasing p_{CO_2} and p_{H_2} , a consequence of the moderate binding strength of the associated intermediates to the catalyst surface, with H₂ and H adsorbing less readily than CO₂ or CO.³⁹ Under blue illumination, the nonthermal CO₂ reaction order remains the same as the thermal reaction order to within experimental uncertainty, suggesting that the surface coverage of CO₂ or CO has a minimal effect on the efficiency of nonthermal reactions. However, the nonthermal H₂ reaction order is much different than the thermal reaction order: for $T_1 = 250 \text{ °C}$, $y = -1.24$ for $I_{\text{blue}} = 3.55 \text{ W cm}^{-2}$ (Figure 5b,d) and $y = -0.87$ for $I_{\text{uv}} = 2.24 \text{ W cm}^{-2}$ (Figure S4). Because of the high thermal conductivity of H₂, it might be argued that increasing p_{H_2} increasingly cools the catalyst, and that is why the reaction slowed. However, if our proposed methodology has completely subtracted all such thermal contributions, the change from a slightly positive reaction order for thermal reactions to a strongly negative reaction order for nonthermal reactions indicates that hydrogen has a profound effect on the nonthermal contribution to the reaction. Since hydrogen surface coverage depends on p_{H_2} ,²⁰ surface hydrogen appears to poison the nonthermal reaction but not the thermal reaction.

Why does the addition of hydrogen quench the nonthermal reaction? Consider that in situ infrared measurements under working CO₂ methanation conditions indicate the dominant surface intermediates on Rh catalysts are CO and H.^{22,24} Assuming CH–O dissociation is the RDS, the reaction order may be deduced from the rate equation

$$R = \frac{(K_1 K_3 K_5 k_4 k_6 / 2)^{1/2} K_2^{3/4}}{[1 + K_2^{1/2} p_{\text{H}_2}^{1/2} + (K_1 K_2^{1/2} K_5 k_6 / 2 K_3 k_4)^{1/2} p_{\text{CO}_2}^{1/2} p_{\text{H}_2}^{1/4}]^2} p_{\text{CO}_2}^{1/2} p_{\text{H}_2}^{3/4} \quad (3)$$

where $K_2^{1/2} p_{\text{H}_2}^{1/2}$ and $(K_1 K_2^{1/2} K_5 k_6 / 2 K_3 k_4)^{1/2} p_{\text{CO}_2}^{1/2} p_{\text{H}_2}^{1/4}$ are proportional to the surface coverage of H and CO, respectively. Thus, the most negative reaction order possible for H₂ is only -0.25 , which occurs when the surface is saturated with hydrogen. The surface is not saturated with hydrogen for

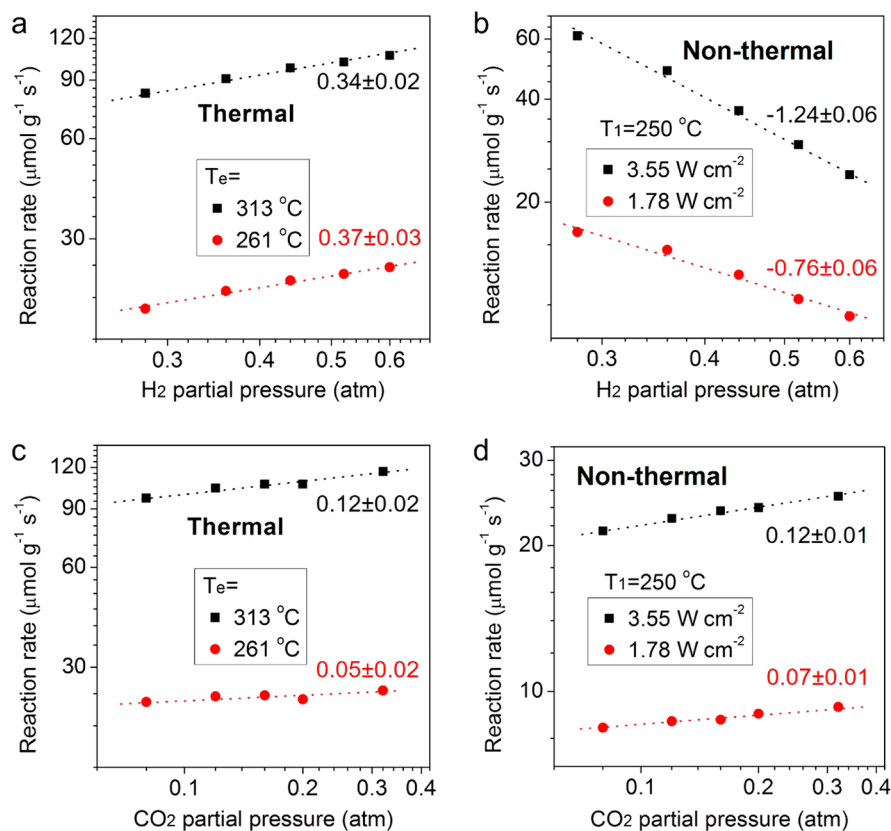


Figure 5. Reaction order of thermal and nonthermal reactions. (a) Hydrogen-dependent thermal reaction rates at $T_e = 313\text{ }^\circ\text{C}$ (black squares) and $261\text{ }^\circ\text{C}$ (red circles) as a function of p_{H_2} , (b) Hydrogen-dependent nonthermal reaction rates at $T_1 = 250\text{ }^\circ\text{C}$ for $I_{\text{blue}} = 3.55$ (black squares) and 1.78 W cm^{-2} (red circles) as a function of p_{H_2} , (c) CO_2 -dependent thermal reaction rates at $T_e = 313\text{ }^\circ\text{C}$ (black squares) and $261\text{ }^\circ\text{C}$ (red circles) as a function of p_{CO_2} , (d) CO_2 -dependent nonthermal reaction rates at $T_1 = 250\text{ }^\circ\text{C}$ for $I_{\text{blue}} = 3.55$ (black squares) and 1.78 W cm^{-2} (red circles) as a function of p_{CO_2} . The total flow rate of CO_2 , H_2 , and Ar is 250 sccm. The CO_2 flow rate is fixed at 40 sccm in parts a and b, and the H_2 flow rate is fixed at 150 sccm in parts c and d. Error bars are smaller than symbols and represent the standard deviations of measurements by the mass spectrometer.

positive reaction orders, such as the thermal reaction with $y = 0.34$. Rate equations derived for other possible mechanisms (through CH_2O or CO dissociation)^{23,24,40} and different assumptions about the RDS can only produce a H_2 reaction order for a hydrogen-rich surface as negative as -0.5 . (See the Supporting Information for details.) Thus, the rate equations alone cannot explain experimentally observed nonthermal reaction orders as negative as -1.24 , so another possibility must be considered. One clue comes from the observation that the H_2 reaction order becomes more negative as illumination intensity increases, which suggests a change in surface coverage with an increasing light intensity.

Assuming that the nonthermal reactions are caused by the transfer of plasmonically excited hot electrons to the antibonding orbital of the critical CH-O intermediate, we use density functional theory (DFT) calculations to explore how its electron-accepting capability may be affected by the dominant surface intermediates (H and CO). We calculated the local density of states (LDOS) for two CHO intermediates adsorbed on a Rh(100) facet separated in turn by a bare Rh surface, two CO molecules, and two H atoms (detailed structures in the Supporting Information, Figure S5), all optimized to their most stable configurations. When C–O antibonding orbitals accept hot electrons, the effective C–O bond order is decreased and its bond dissociation energy

lowered, thus activating the CHO intermediate to accelerate CH_4 production.¹⁶ In all cases, obvious peaks at $\sim 2.3\text{ eV}$ above the Fermi level in the LDOS plot are observed (Figure 6a), indicating the intense antibonding bands of the C–O bond in CHO intermediates. The insertion of CO molecules in the space between CHO intermediates only slightly lowers the LDOS associated with their C–O antibonding orbitals, as shown by a $\sim 15\%$ decrease in the LDOS of the C(pz) orbitals. By contrast, inserting atomic hydrogen significantly decreases the LDOS and a decrease of $\sim 50\%$ in the LDOS of the C(pz) orbitals is observed, thereby reducing the ability of CHO intermediates to accept hot electrons from the Rh nanoparticles. Implicitly, these calculations reveal that C–O antibonding orbitals can delocalize and be distributed among these two CHO intermediates, regardless of whether they are separated by the bare Rh surface or other adsorbates (Figure 6b and Figure S6).⁴¹ This implies that some plasmonically generated hot electrons transferred from the Rh nanoparticle may simultaneously weaken several C–O bonds in nearby proximal CHO intermediates, thus inducing the formation of multiple product CH_4 molecules. It has even been proposed that after inducing reactions, hot electrons may dissipate their excess energy by re-emission of photons which can be reabsorbed to increase the efficiency of plasmon-enhanced catalysis.⁴ The delocalization of hot electrons among two or

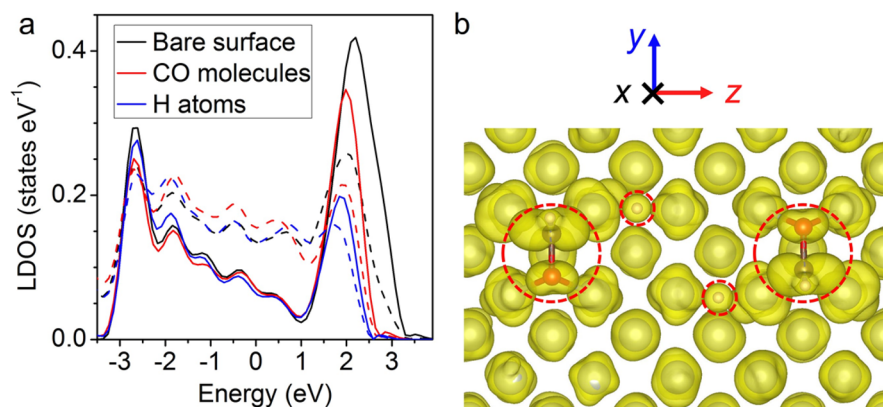


Figure 6. (a) LDOS of C–O antibonding bands (solid lines for C(pz) orbitals, dashed lines for O(pz) orbitals) of two CHO adsorbates on a Rh(100) facet separated by a bare Rh surface (black), CO molecules (red), and H atoms (blue) in between. The obvious decrease of π^* antibonding bands at ~ 2.3 eV (above the Fermi level) with the insertion of H atoms explains the negative reaction order on H_2 of nonthermal reactions. (b) Top view of the distribution of a C–O π^* antibonding orbital consisting of two CHO adsorbates (circled) separated by two H atoms (circled). The majority of probability density locates evenly on the two CHO adsorbates, indicating the delocalization of antibonding orbitals among them. Part of probability density is found on H atoms and Rh atoms interacting with the CHO adsorbates.

more critical intermediates helps explain the high nonthermal AQE, while the sensitivity of the LDOS on proximal atomic hydrogen may explain the negative reaction order for p_{H_2} .

In conclusion, we introduce a methodology to distinguish the thermal, photothermal, and nonthermal contributions from an illuminated, plasmon-enhanced catalyst composed of Rh nanoparticles on a TiO_2 support. The model correctly extracts the effective thermal and nonthermal reaction rates under illumination by simultaneously measuring the total reaction rate and the top- and bottom-surface temperatures of the catalyst bed. The nonthermal reaction rate grows with a superlinear dependence on illumination intensity, while the AQE of plasmon-enhanced CO_2 methanation reaches $\sim 46\%$ on the Rh- $/TiO_2$ catalyst for a top-surface temperature of $350^\circ C$, a result wrought by engineering the catalyst support and morphology of Rh nanoparticles to reduce the nonthermal activation energy of the RDS. Unlike the thermal reaction, the nonthermal reaction rate is quenched with increasing p_{H_2} , explained by DFT calculations that indicate nearby hydrogen inhibits the ability of the critical CHO adsorbates to accept hot electrons. Although it complicates the understanding of the reaction mechanisms, photoheating accelerates chemical reactions. In fact, and unlike in traditional photocatalysis, heat and light work synergistically in these reactions: the higher the temperature, the higher the efficiency in plasmon-enhanced catalysis. By this, one may envision that the entire solar spectrum can be used to its full potential, with a portion of the spectrum providing photoheating while another promoting nonthermal reactions.

Methods. Photocatalyst Preparation. Rh nanospheres and nanocubes are synthesized by polyol methods. For Rh nanospheres, 25 mg of polyvinylpyrrolidone (PVP, MW ≈ 55000 , Aldrich) was dissolved in 5.6 mL of ethylene glycol (EG, J. T. Baker) in a 20 mL glass vial, and the mixture was stirred in an oil bath at $160^\circ C$ for 30 min. A total of 12 mg of rhodium(III) chloride hydrate ($RhCl_3 \cdot xH_2O$, 40% Rh, Pressure Chemical) was separately dissolved in 0.4 mL of EG and quickly injected into the hot solution to initiate nanoparticle growth. The reaction mixture was stirred for another 30 min and then cooled to room temperature. The Rh nanocubes were synthesized by a modified slow-injection polyol method.¹⁷ 54 mg of potassium bromide (KBr, ACS, Acros) was dissolved in 2

mL of EG in a 20 mL glass vial, and the mixture was stirred in an oil bath at $160^\circ C$ for 1 h. A total of 12 mg of $RhCl_3 \cdot xH_2O$ and 25 mg of PVP were dissolved in 2 mL of EG separately, and the mixture was injected into the hot reaction mixture by a two-channel syringe pump at a rate of 1 mL h^{-1} . The injection was paused for 15 min after adding $20\ \mu\text{L}$ of the Rh precursor. After complete injection of the precursor, the reaction mixture was stirred for another 30 min and then cooled to room temperature.

The solution of Rh nanoparticles was washed with deionized water/acetone until no Cl^- and Br^- were detected in the supernatant. The nanoparticles were dispersed in 20 mL of ethanol, and the mixture was impregnated on ~ 95 mg of oxide supports to achieve ~ 5 wt % Rh loading. The oxide supports were Al_2O_3 (Degussa, Alu Oxide C, specific surface area $85\text{--}115\text{ m}^2\text{ g}^{-1}$) and TiO_2 (Degussa, P25, specific surface area $35\text{--}65\text{ m}^2\text{ g}^{-1}$). The supports were activated in air at $500^\circ C$ for 5 h before impregnation. Upon evaporation of the solvent, the obtained solid was ground and calcined in air at $400^\circ C$ for 2 h.

Both thermocouples were embedded just within the photocatalyst so that they accurately measured local temperature and avoided direct photothermal heating.

Reactor Setup and Photocatalytic Reactions. The photocatalytic reaction was carried out in a custom-built gaseous reaction system. The system consisted of a gas delivery system, a fixed-bed stainless-steel reactor equipped with a quartz window and a programmable temperature controller, LED light sources, and an online mass spectrometer, as described in detail previously.¹⁶ 10–30 mg of Rh photocatalysts were loaded in the reactor to fill a 4 mm height and 6 mm diameter catalyst cup and ensure complete absorption of light for the catalytic measurements. H_2 (UHP), CO_2 (research grade), and Ar (UHP) compressed gas tanks were obtained from Airgas. The Rh photocatalysts were first reduced under 60 mL min^{-1} H_2 and 40 mL min^{-1} Ar at $350^\circ C$ for 2 h, and then the gas flow was switched to a mixture of CO_2 , H_2 , and Ar with the desired ratio and a total flow rate of 250 mL min^{-1} . The detection limit of the mass spectrometer is $\sim 0.001\%$ conversion of CO_2 . For each temperature and light intensity condition, at least 15 min elapsed before reaching steady state, and seven sequential measurements were made to determine the steady-state

concentration of each gas and the associated reaction rates and uncertainties.

Calculation of the Penetration Depth. The penetration depth (δ) is defined as the depth at which the intensity of the radiation inside the material falls to $1/e$ of its original value. The penetration depth for an electromagnetic wave at normal incidence is given by

$$\frac{1}{\delta} = \frac{4\pi}{\lambda} k$$

where λ is the wavelength of the illuminating electromagnetic field and k is the imaginary part of the refractive index of the material, which can be calculated from its effective dielectric function. To obtain k , the catalyst is modeled as an oxide host with inclusions of dipolar metallic NPs (Rh spheres or cubes) using the Maxwell-Garnett effective medium theory.⁴² The effective dielectric function (ϵ_{eff}) is thereby given through

$$\frac{\epsilon_{\text{eff}} - \epsilon_{\text{h}}}{\epsilon_{\text{eff}} + 2\epsilon_{\text{h}}} = f \frac{\epsilon_{\text{i}} - \epsilon_{\text{h}}}{\epsilon_{\text{i}} + 2\epsilon_{\text{h}}}$$

where ϵ_{h} and ϵ_{i} are the dielectric functions of the host oxide⁴³ and Rh inclusions,⁴⁴ respectively. f is the volume density of inclusions embedded in the host, derived for each experimental configuration from the weight percentage of Rh (wt %) considering the Rh NP volumes and the Rh and oxide densities. From the value ϵ_{eff} , k is calculated through $k = \text{Im}(\sqrt{\epsilon_{\text{eff}}})$ to estimate the penetration depth.

DFT Calculations. All of the periodic boundary condition (PBC) calculations in this work were performed with the Vienna Ab initio Simulation Package (VASP).⁴⁵ The Perdew–Burke–Ernzerhof (PBE)⁴⁶ exchange–correlation (xc) functional was used along with its corresponding projected augmented wave (PAW) pseudopotentials. The semiempirical D2 model⁴⁷ was applied to describe the van der Waals interactions. A plane-wave cutoff of 500 eV was chosen. The Γ -centered $2 \times 3 \times 1$ k-point grid was used for the structural relaxations (converged to 0.01 eV \AA^{-1}) and $8 \times 12 \times 1$ for the projected LDOS calculations and for the plotting of band densities. Periodic boundary conditions were used in all three directions for the *fcc* Rh model. A vacuum of $>15 \text{ \AA}$ was used in the *x*-direction to separate the Rh(100) surface slabs (parallel to the *yz*-plane) containing 4 layers of Rh atoms. The two adsorbed CHO groups separated by a bare Rh surface, two H groups, and two CO groups were placed on the exposed Rh(100) surface. The optimized structures of the supercell models are generated with GaussView.⁴⁸ The band density plots are produced with VESTA.⁴⁹

Material Characterization. Transmission electron microscopy (TEM) images were collected by a FEI Tecnai G² Twin operating at 200 kV. The TEM samples were prepared by dispersing the photocatalysts in ethanol with sonication and depositing on a copper grid coated with a carbon film (Ted Pella, 01813). Diffuse reflectance ultraviolet–visible extinction spectra were obtained on an Agilent Cary 5000 equipped with an external diffuse reflectance accessory (DRA-2500). The composition of the photocatalysts was measured by a Kratos Analytical Axis Ultra X-ray Photoelectron Spectrometer (XPS).

■ ASSOCIATED CONTENT

§ Supporting Information

The Supporting Information is available free of charge on the ACS Publications website at DOI: 10.1021/acs.nanolett.7b04776.

Reaction mechanism and rate equation of CO₂ methanation on Rh catalysts, calculation of apparent activation energy, TEM image and reaction rates of Rh catalysts, and DFT calculations of reaction intermediates on the Rh surface (PDF)

■ AUTHOR INFORMATION

Corresponding Author

*E-mail: j.liu@duke.edu.

ORCID

Weitao Yang: 0000-0001-5576-2828

Henry O. Everitt: 0000-0002-8141-3768

Jie Liu: 0000-0003-0451-6111

Notes

The authors declare no competing financial interest.

■ ACKNOWLEDGMENTS

This research is supported by the National Science Foundation (CHE-1565657) and the Army Research Office (Award W911NF-15-1-0320). X.Z. is supported by the Katherine Goodman Stern fellowship from the Graduate School, Duke University. X.L. is supported by the Department of Defense (DoD) through the National Defense Science & Engineering Graduate Fellowship (NDSEG) Program. D.Z., N.Q.S., and W.Y. are supported by the Center for the Computational Design of Functional Layered Materials, an Energy Frontier Research Center funded by the U.S. Department of Energy (DOE), Office of Science, Basic Energy Sciences (BES), under Award DE-SC0012575. Y.G. and F.M. are supported by MICINN (Spanish Ministry of Science and Innovation, project FIS2013-45854-P) and the Army Research Laboratory under Cooperative Agreement no. W911NF-17-2-0023. Y.G. thanks the University of Cantabria for the FPU grant.

■ REFERENCES

- (1) Maier, S. A.; Atwater, H. A. *J. Appl. Phys.* **2005**, *98* (1), 011101.
- (2) Watanabe, K.; Menzel, D.; Nilius, N.; Freund, H.-J. *Chem. Rev.* **2006**, *106* (10), 4301–4320.
- (3) Christopher, P.; Xin, H.; Linic, S. *Nat. Chem.* **2011**, *3* (6), 467–472.
- (4) Christopher, P.; Xin, H.; Marimuthu, A.; Linic, S. *Nat. Mater.* **2012**, *11* (12), 1044–1050.
- (5) Mukherjee, S.; Libisch, F.; Large, N.; Neumann, O.; Brown, L. V.; Cheng, J.; Lassiter, J. B.; Carter, E. A.; Nordlander, P.; Halas, N. J. *Nano Lett.* **2013**, *13* (1), 240–247.
- (6) Linic, S.; Aslam, U.; Boerigter, C.; Morabito, M. *Nat. Mater.* **2015**, *14* (6), 567–576.
- (7) Wu, B.; Lee, J.; Mubeen, S.; Jun, Y.-S.; Stucky, G. D.; Moskovits, M. *Adv. Opt. Mater.* **2016**, *4* (7), 1041–1046.
- (8) Hansen, T. W.; DeLaRiva, A. T.; Challa, S. R.; Datye, A. K. *Acc. Chem. Res.* **2013**, *46* (8), 1720–1730.
- (9) Campbell, C. T.; Parker, S. C.; Starr, D. E. *Science* **2002**, *298* (5594), 811–814.
- (10) Xie, S.; Liu, X. Y.; Xia, Y. *Nano Res.* **2015**, *8* (1), 82–96.
- (11) Chambers, M. B.; Wang, X.; Elgrishi, N.; Hendon, C. H.; Walsh, A.; Bonnefoy, J.; Canivet, J.; Quadrelli, E. A.; Farrusseng, D.; Mellot-Draznieks, C.; Fontecave, M. *ChemSusChem* **2015**, *8* (4), 603–608.

- (12) Hou, C.; Zhao, G.; Ji, Y.; Niu, Z.; Wang, D.; Li, Y. *Nano Res.* **2014**, *7* (9), 1364–1369.
- (13) Zhang, Y.; Grass, M. E.; Kuhn, J. N.; Tao, F.; Habas, S. E.; Huang, W.; Yang, P.; Somorjai, G. A. *J. Am. Chem. Soc.* **2008**, *130* (18), 5868–5869.
- (14) Solymosi, F.; Erdöhelyi, A.; Bánsági, T. *J. Catal.* **1981**, *68* (2), 371–382.
- (15) Sexton, B. A.; Somorjai, G. A. *J. Catal.* **1977**, *46* (2), 167–189.
- (16) Zhang, X.; Li, X.; Zhang, D.; Su, N. Q.; Yang, W.; Everitt, H. O.; Liu, J. *Nat. Commun.* **2017**, *8*, 14542.
- (17) Zhang, X.; Li, P.; Barreda, Á.; Gutiérrez, Y.; González, F.; Moreno, F.; Everitt, H. O.; Liu, J. *Nanoscale Horiz.* **2016**, *1* (1), 75–80.
- (18) Watson, A. M.; Zhang, X.; Alcaraz de la Osa, R.; Sanz, J. M.; González, F.; Moreno, F.; Finkelstein, G.; Liu, J.; Everitt, H. O. *Nano Lett.* **2015**, *15* (2), 1095–1100.
- (19) Sanz, J. M.; Ortiz, D.; Alcaraz de la Osa, R.; Saiz, J. M.; González, F.; Brown, A. S.; Losurdo, M.; Everitt, H. O.; Moreno, F. *J. Phys. Chem. C* **2013**, *117* (38), 19606–19615.
- (20) Avanesian, T.; Gusmão, G. S.; Christopher, P. *J. Catal.* **2016**, *343*, 86–96.
- (21) Karelavic, A.; Ruiz, P. *J. Catal.* **2013**, *301*, 141–153.
- (22) Jacquemin, M.; Beuls, A.; Ruiz, P. *Catal. Today* **2010**, *157* (1–4), 462–466.
- (23) Williams, K. J.; Boffa, A. B.; Salmeron, M.; Bell, A. T.; Somorjai, G. A. *Catal. Lett.* **1991**, *9* (5–6), 415–426.
- (24) Henderson, M. A.; Worley, S. D. *J. Phys. Chem.* **1985**, *89* (8), 1417–1423.
- (25) Mukherjee, S.; Zhou, L.; Goodman, A. M.; Large, N.; Ayala-Orozco, C.; Zhang, Y.; Nordlander, P.; Halas, N. J. *J. Am. Chem. Soc.* **2014**, *136* (1), 64–67.
- (26) Narang, P.; Sundararaman, R.; Atwater, H. A. *Nanophotonics* **2016**, *5* (1), 96.
- (27) Demichel, O.; Petit, M.; Viarbitskaya, S.; Méjard, R.; de Fornel, F.; Hertz, E.; Billard, F.; Bouhelier, A.; Cluzel, B. *ACS Photonics* **2016**, *3* (5), 791–795.
- (28) Brown, A. M.; Sundararaman, R.; Narang, P.; Goddard, W. A.; Atwater, H. A. *ACS Nano* **2016**, *10* (1), 957–966.
- (29) Christensen, N. E. *Phys. Status Solidi B* **1973**, *55* (1), 117–127.
- (30) Marimuthu, A.; Zhang, J.; Linic, S. *Science* **2013**, *339* (6127), 1590–1593.
- (31) Kale, M. J.; Avanesian, T.; Christopher, P. *ACS Catal.* **2014**, *4* (1), 116–128.
- (32) Olsen, T.; Schiøtz, J. *Phys. Rev. Lett.* **2009**, *103* (23), 238301.
- (33) Swearer, D. F.; Zhao, H.; Zhou, L.; Zhang, C.; Robotjazi, H.; Martinez, J. M. P.; Krauter, C. M.; Yazdi, S.; McClain, M. J.; Ringe, E.; Carter, E. A.; Nordlander, P.; Halas, N. J. *Proc. Natl. Acad. Sci. U. S. A.* **2016**, *113* (32), 8916–8920.
- (34) Xiao, Q.; Sarina, S.; Waclawik, E. R.; Jia, J.; Chang, J.; Riches, J. D.; Wu, H.; Zheng, Z.; Zhu, H. *ACS Catal.* **2016**, *6* (3), 1744–1753.
- (35) Kale, M. J.; Avanesian, T.; Xin, H.; Yan, J.; Christopher, P. *Nano Lett.* **2014**, *14* (9), 5405–5412.
- (36) Wu, K.; Chen, J.; McBride, J. R.; Lian, T. *Science* **2015**, *349* (6248), 632–635.
- (37) Knight, M. W.; Sobhani, H.; Nordlander, P.; Halas, N. J. *Science* **2011**, *332* (6030), 702–704.
- (38) Zhang, Z. L.; Kladi, A.; Verykios, X. E. *J. Catal.* **1994**, *148* (2), 737–747.
- (39) Castner, D. G.; Sexton, B. A.; Somorjai, G. A. *Surf. Sci.* **1978**, *71* (3), 519–540.
- (40) Eckle, S.; Anfang, H.-G.; Behm, R. J. *J. Phys. Chem. C* **2011**, *115* (4), 1361–1367.
- (41) Cabalo, J.; Guicheteau, J. A.; Christesen, S. *J. Phys. Chem. A* **2013**, *117* (37), 9028–9038.
- (42) Garnett, J. C. M. *Philos. Trans. R. Soc., A* **1906**, *205* (387–401), 237–288.
- (43) DeVore, J. R. *J. Opt. Soc. Am.* **1951**, *41* (6), 416–419.
- (44) Palik, E.; Bennett, J. M. *Handbook of Optical Constants of Solids I and II*; Academic Press: New York, 1995.
- (45) Kresse, G.; Furthmüller, J. *Phys. Rev. B: Condens. Matter Mater. Phys.* **1996**, *54* (16), 11169–11186.
- (46) Perdew, J. P.; Burke, K.; Ernzerhof, M. *Phys. Rev. Lett.* **1996**, *77* (18), 3865–3868.
- (47) Grimme, S. *J. Comput. Chem.* **2006**, *27* (15), 1787–1799.
- (48) Dennington, R.; Keith, T. A.; Millam, J. M. *GaussView*, Version 5; Semichem Inc.: Shawnee Mission, KS, 2009.
- (49) Momma, K.; Izumi, F. *J. Appl. Crystallogr.* **2011**, *44* (6), 1272–1276.